Electronic Supplementary Information

Chalcogen Alloying Mediated Electronic Structure Modulation in $Nb(S_xSe_{(1-x)})_2$ Nanosheets for Hydrogen Evolution Reaction

Varsha Jha [a], Md. Samim Hassan [a], Ankita Kumari [a], Shubham Kumar [a], Sahil Singh [a], Jyoti Yadav[a], Dibyajyoti Ghosh,[a,b,#] and Sameer Sapra[a,]*

[a]*Department of Chemistry, Indian Institute of Technology Delhi, Hauz Khas, New Delhi 110016, India*

[b]*Department of Materials Science and Engineering, Indian Institute of Technology Delhi, Hauz Khas, New Delhi 110016*

**Email: sapra@chemistry.iitd.ac.in*

 # Email: dibyajyoti.ghosh@mse.iitd.ac.in

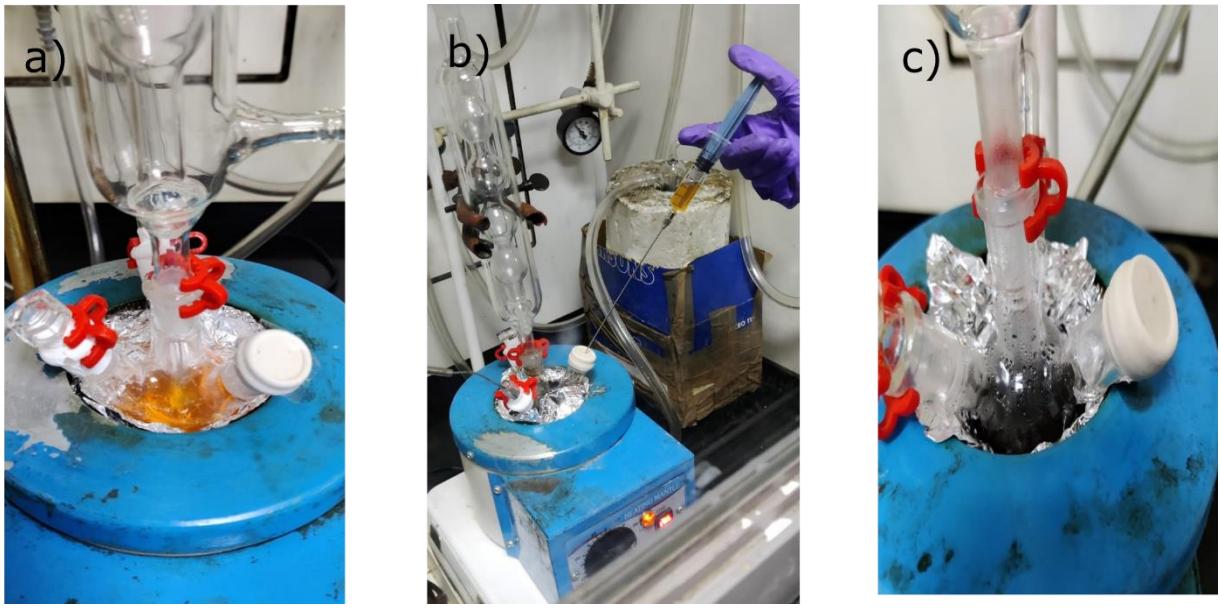

Fig. S1 (a) color of precursor solution containing $(PhCH_2)_2Se_2$/$(PhCH_2)_2S_2$, $NbCl_5$ and oleyl amine (OLAM); (b) dropwise injection of precursor solution into pre-heated OLAM solution kept at 300 °C; (c) color change to black upon precursor injection.

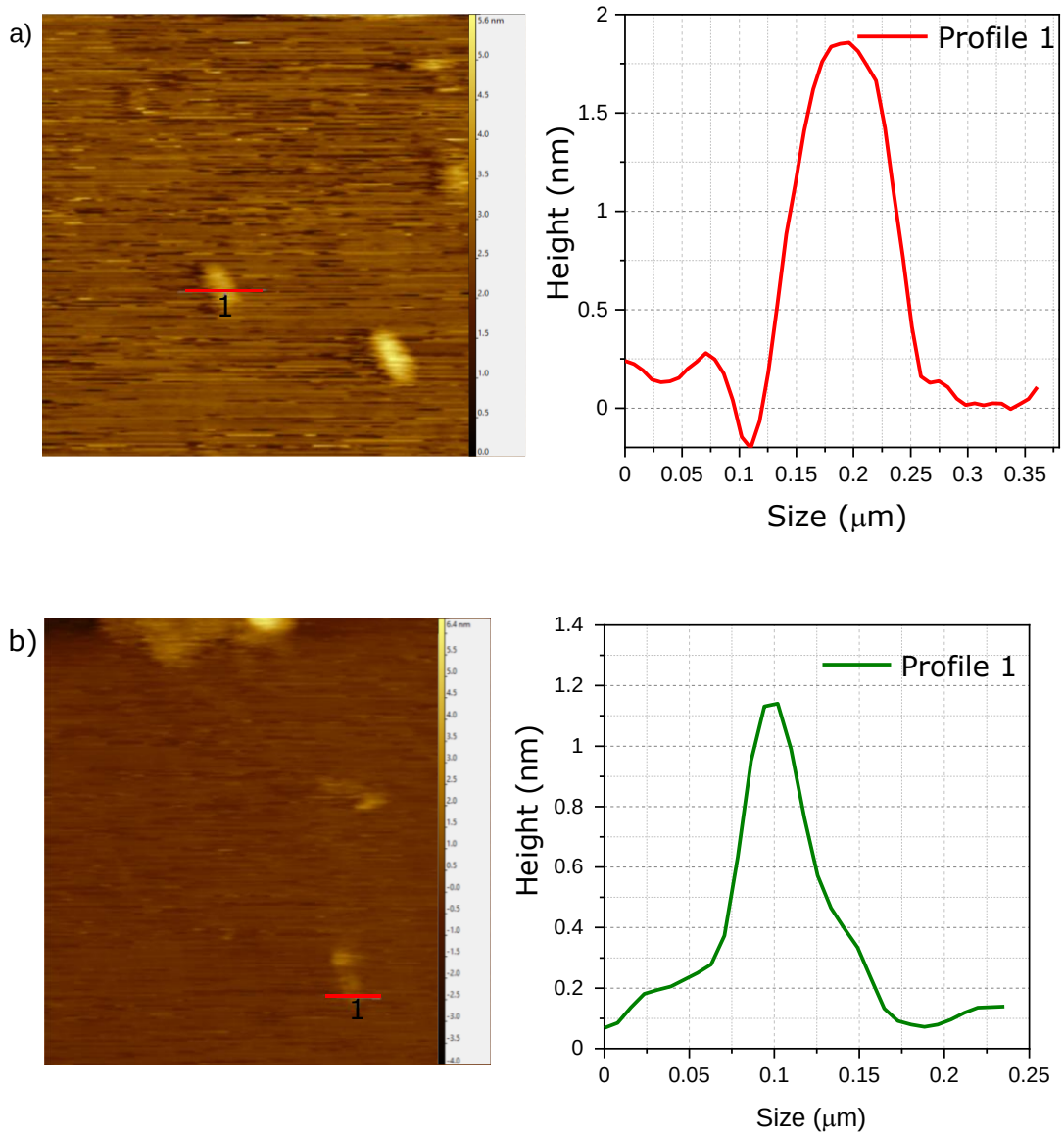

Fig. S2 AFM images: (a) $NbSe_2$; (b) NbS_2 nanosheets. For $NbSe_2$, height profile is 1.8 nm, confirming 2 layers thickness. Whereas for NbS_2 it is 1.2 nm which confirms approximately 1 layer thickness, considering the presence of OLAM ligand (0.5 nm)[1]. This confirms the transformation from monolayer to bilayer thickness, along c-axis with increasing Se content.

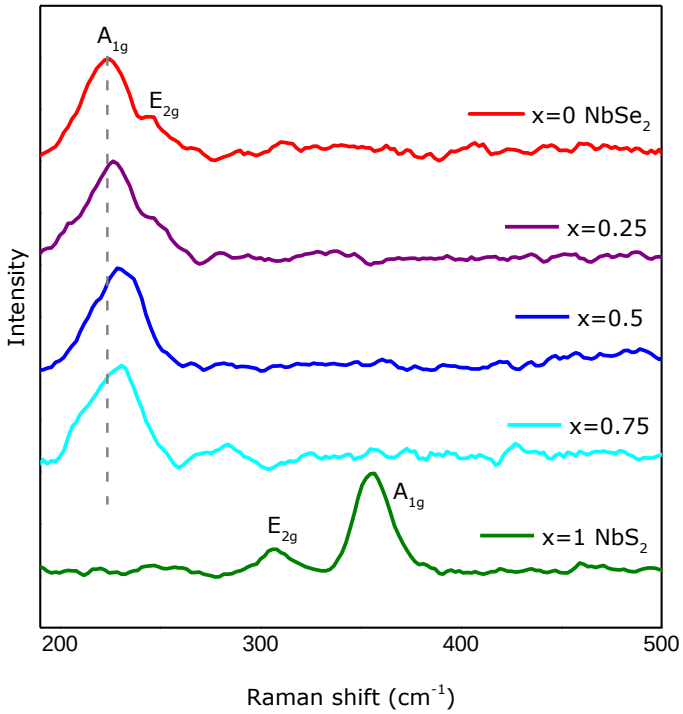

Fig. S3 Raman spectra of $Nb(S_xSe_{(1-x)})_2$ NSs under 532nm laser.

To comprehend the structure of $Nb(S_xSe_{(1-x)})_2$, Raman spectra were collected under a 532 nm laser. It displays two vibration modes with Nb-Se modes at a lower frequency than Nb-S modes. The spectrum for $NbSe_2$ shows contribution from two peaks, i.e., in-plane E_{2g} mode (245 cm^{-1}) and out-of-plane A_{1g} mode (225 cm^{-1}) vibrations.[2] With initial x = 0.25 doping of S, there is slight shift towards the higher wavenumber observed due the softening of Nb-Se modes. For x=0.25, 0.5 and 0.75 there is dominance of Nb-Se modes compared to Nb-S modes which is indicative of relatively higher Se concentration in $Nb(S_xSe_{(1-x)})_2$.[3] Complete substitution of Se with S in NbS_2 features peaks at 307 cm^{-1} and 355 cm^{-1} assignable to E_{2g} and A_{1g} modes, respectively.[4]

x = 0
$NbSe_2$

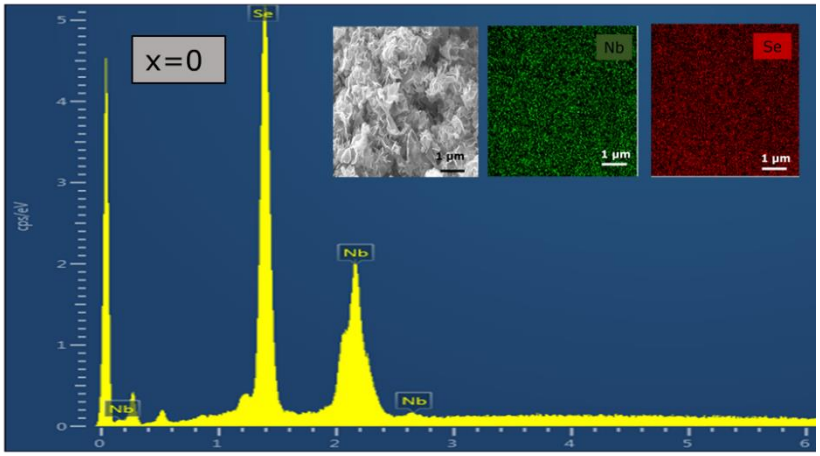

x = 0.25
$NbS_{1/2}Se_{2/3}$

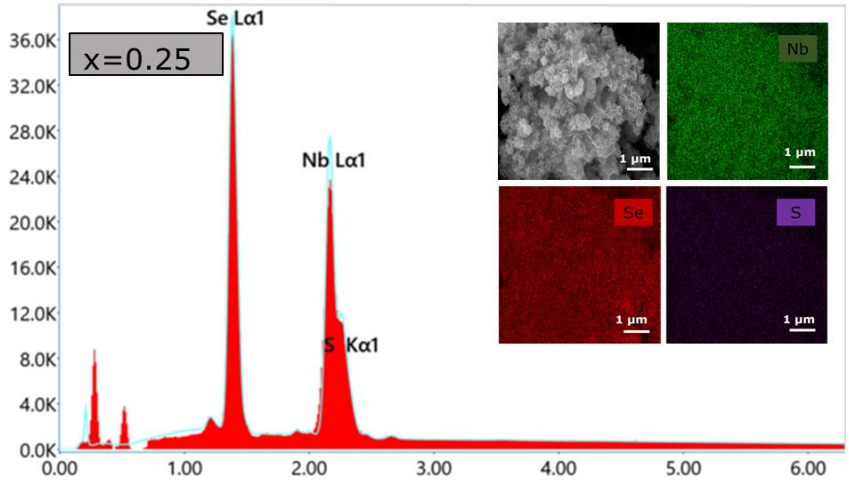

x = 0.75
$NbS_{2/3}Se_{1/2}$

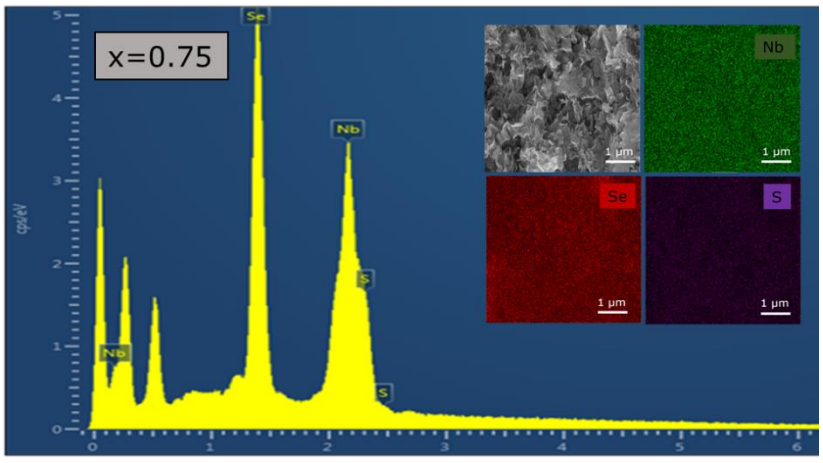

x = 1

NbS_2

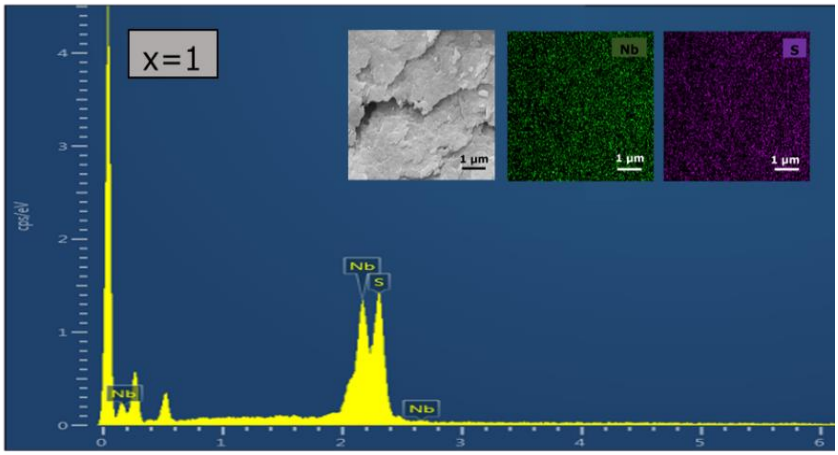

Fig. S4 FE-SEM based corresponding elemental distribution maps and spectrum showing uniform distribution of Nb, Se and S of x = 0; 0.25; x = 0.75; x = 1. The FE-SEM image shows sheet type surface morphology. EDX spectrum exhibits relatively high atomic percentage of Se w.r.t. S.

Loaded composition	**EDX Composition**		
	At. % of Nb	**At. % of S**	**At. % of Se**
X = 0 ($NbSe_2$)	36.46	-	63.54
X = 0.25 ($NbS_{1/2}Se_{3/2}$)	38.1	3.12	58.2
X = 0.5 (NbSSe)	37.9	9.31	46.24
X = 0.75 ($NbS_{3/2}Se_{1/2}$)	37.5	15.47	39.8
X = 1 (NbS_2)	43.64	56.36	-

Table S1 S:Se ratios of loaded composition and FE-SEM EDX elemental mapping for all compositions highlighting the actual S content is lesser compared to the nominal amounts. To explain this observation, we propose the reason to be difference in rate of decomposition of the

chalcogen precursors with C-S bond being relatively stronger than C-Se bond (Bond dissociation energy: C-S: 699 KJ/mol and C-Se: 582 KJ/mol)[5] and hence lesser S goes into the lattice than feed in amounts.

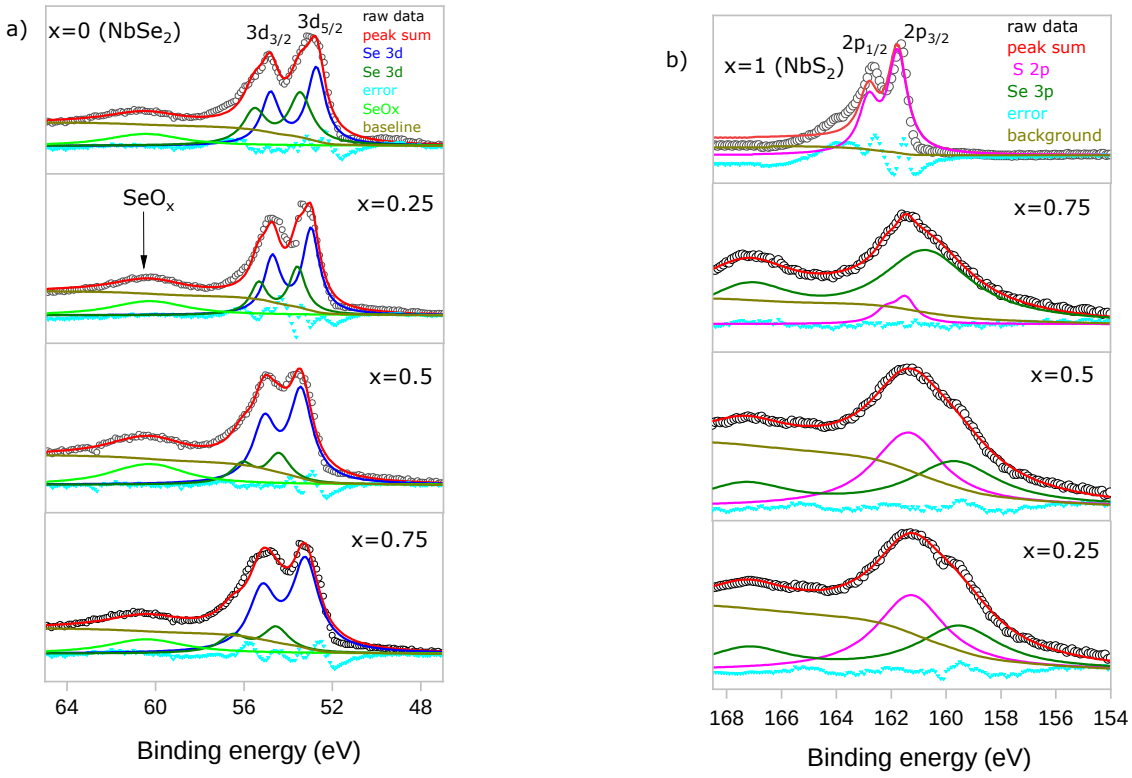

Fig. S5 high resolution XPS spectra of (a) Se - 3d spectra shows two peaks at 53.01 and 54.94 eV corresponding to $3d_{5/2}$ and $3d_{3/2}$ binding energies.[6,7] The 3d spectra of Se can be deconvoluted into two doublets possibly due to presence of Se intermediates left over from the decomposition of $(PhCH_2)_2Se_2$.[8] Also, there is peak due to SeO_x in all compositions; (b) S-2p spectra.

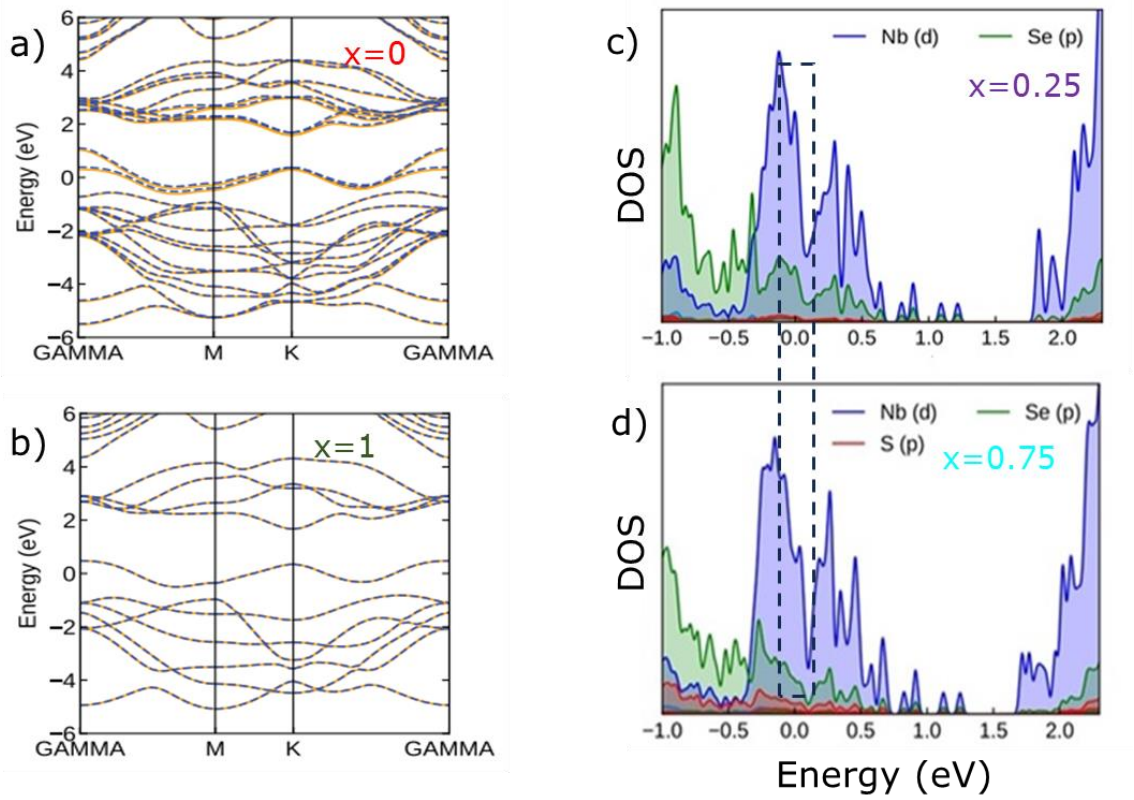

Fig. S6 (a,b) band plots of bilayer $NbSe_2$ and monolayer NbS_2; (c,d) DOS plots of x=0.25, x=0.75 for $Nb(S_xSe_{(1-x)})_2$ showing variation in d band contribution at fermi level with chalcogen variation.

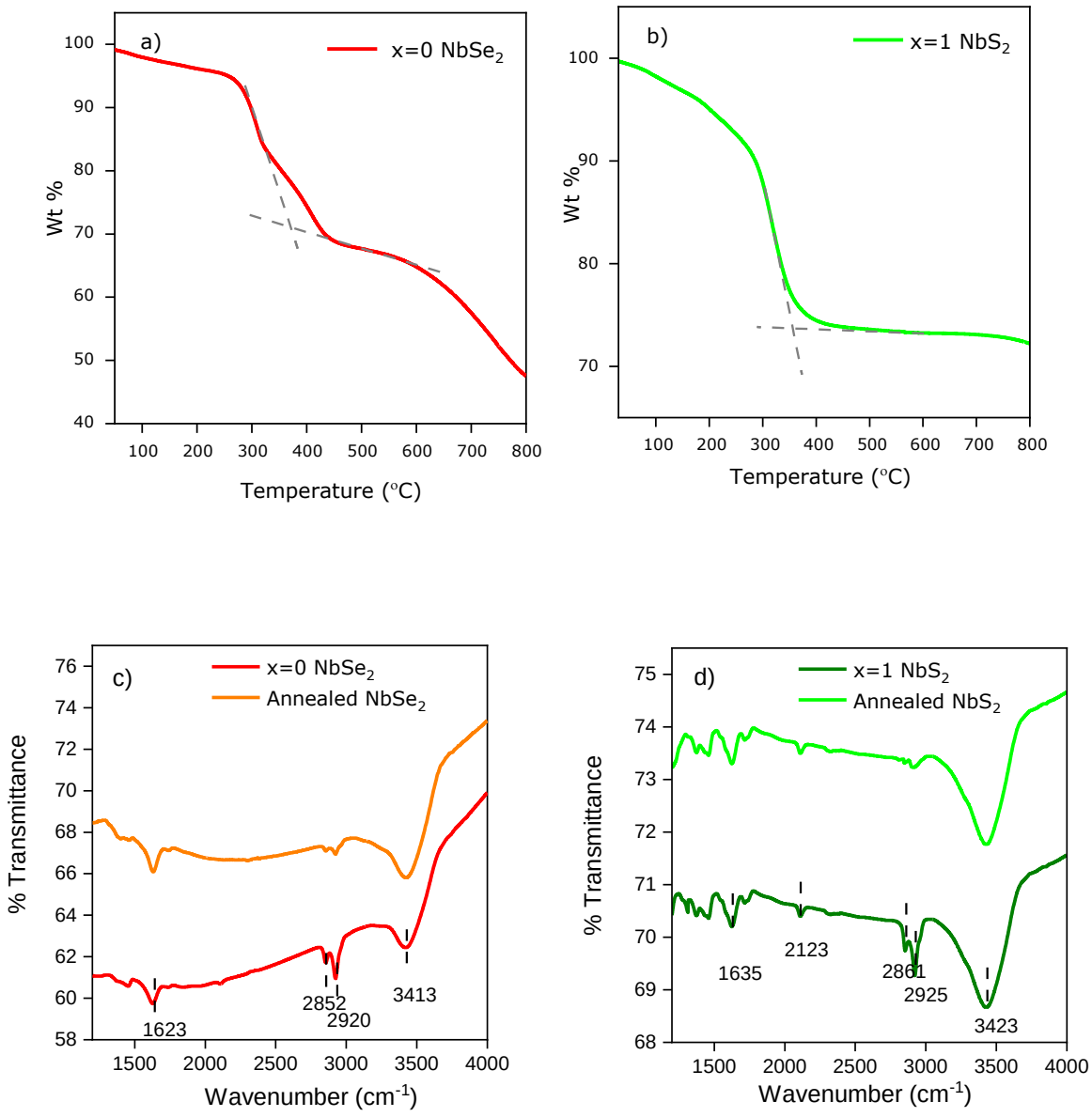

Fig. S7 (a,b) TGA curves of $NbSe_2$ and NbS_2 nanosheets (NSs) respectively showing approximately 30% loss in the molecular weight at 368°C corresponding to loss due to surface OLAM ligand. Surface ligands were removed to enhance the conductivity; (c,d) FTIR spectra of $NbSe_2$ and NbS_2 NSs respectively, before and after annealing at 500°C. All other compositions were also annealed at 500°C for electrochemical studies.

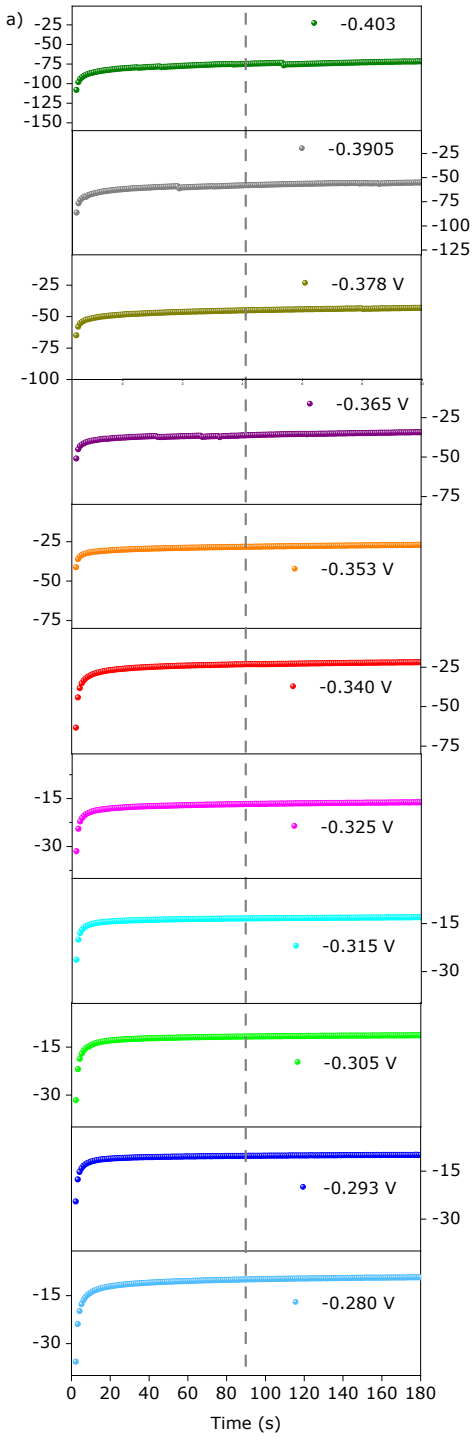
a)
-0.403
-0.3905
-0.378 V
-0.365 V
-0.353 V
-0.340 V
-0.325 V
-0.315 V
-0.305 V
-0.293 V
-0.280 V
Time (s)

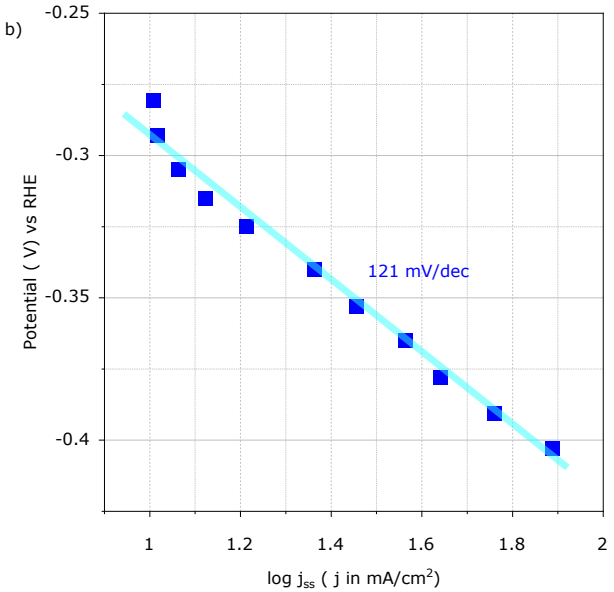
b)
121 mV/dec
Potential (V) vs RHE
log j$_{ss}$ (j in mA/cm^2)

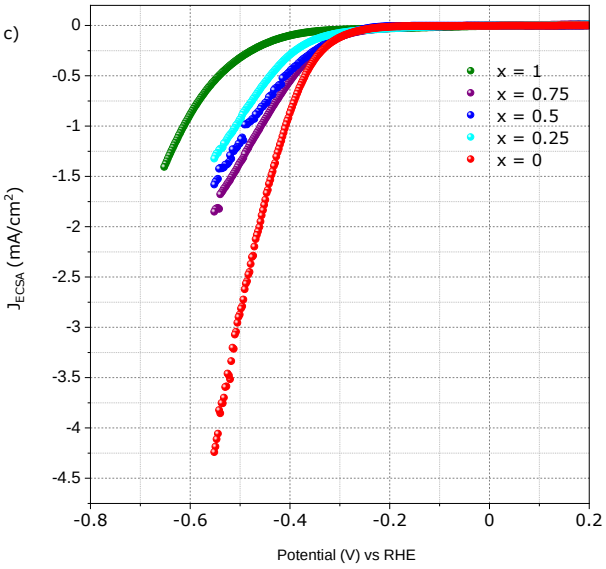
c)
x = 1
x = 0.75
x = 0.5
x = 0.25
x = 0
J$_{ECSA}$ (mA/cm^2)
Potential (V) vs RHE

Fig. S8 (a) For x = 0.5 (NbSSe), chronoamperometry response at different potentials referenced w.r.t. RHE; (b) corresponding linear fit of steady state current density at 90th second gives the tafel slope of 121mV/dec for x = 0.5 composition; (c) LSV curves with current density normalized w.r.t ECSA showing high intrinsic conductivity of x = 0.5 composition.

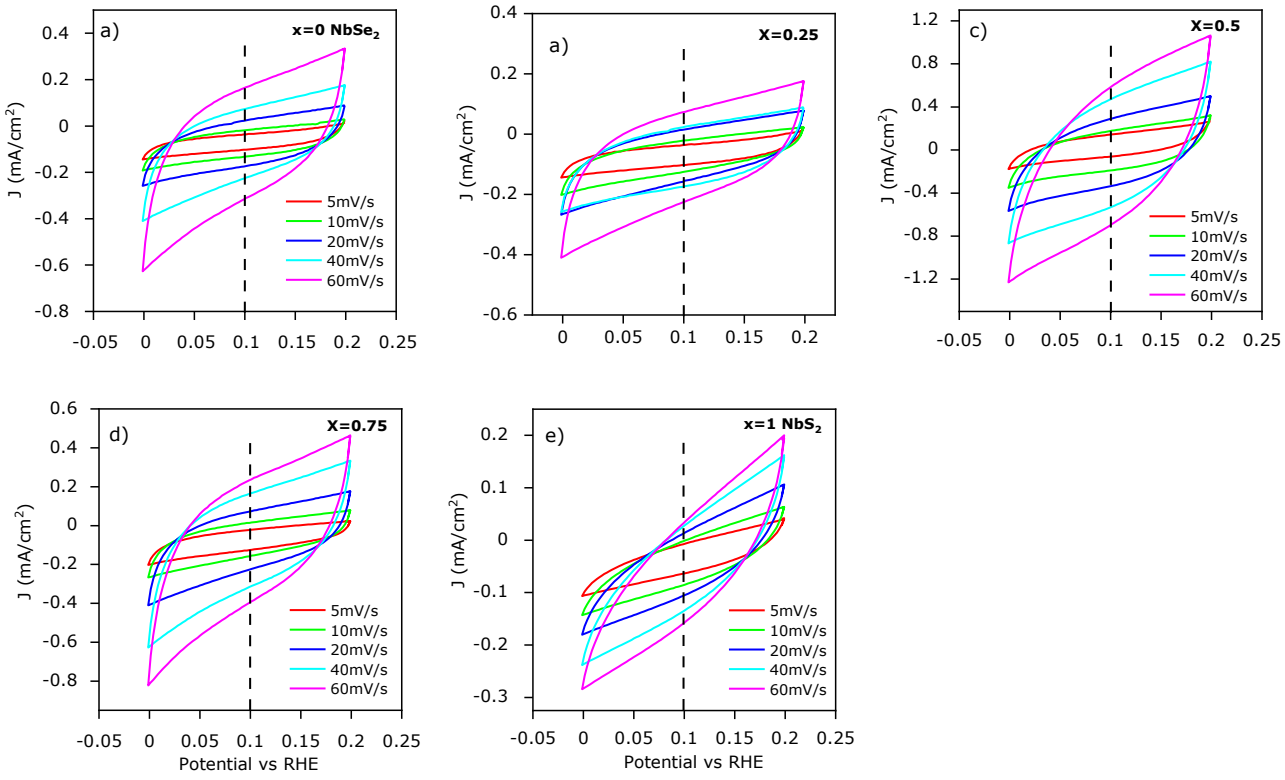

Fig. S9 (a-e) Cyclic voltametric curves of $Nb(S_xSe_{(1-x)})_2$ for x = 0, 0.25, 0.5, 0.75, 1. CV for all compositions of 2D $Nb(S_xSe_{(1-x)})_2$ NSs were collected in the non-faradaic potential window i.e., 0 – 0.2V vs RHE at scan rates 5 mV /s, 10 mV /s, 20 mV/s, 40 mV/s and 60 mV/s.

ECSA calculations:

Cyclic voltammetry curves were collected in the non-faradaic region. Half of the difference in the anodic and cathodic current densities at the intermediate value of CV curves (i.e. 0.1 V) was plotted as a function of scan rate. Linear fitting of the graph gives double layer capacitance (Cdl). Cdl values are a direct measure of the electrochemical surface area.[9,10]

$$ECSA = {}^{C_{dl}}/_{C_s}$$

C_s is the specific capacitance, the value of which is 40 $\mu F cm^{-2}$ $per\ cm^2_{ECSA}$

Electrochemical Impedance fitting parameters:

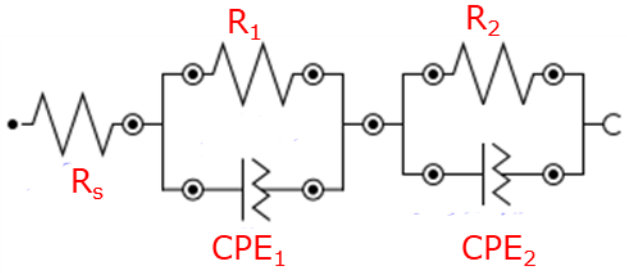

	X = 0 $NbSe_2$	**X = 0.25 $NbS_{1/2}Se_{3/2}$**	**X = 0.5 NbSSe**	**X = 0.75 $NbS_{3/2}Se_{1/2}$**	**X = 1 NbS_2**
R_s	14.8 Ω	24.1 Ω	6.42 Ω	10.2 Ω	30.3 Ω
R_{ct} (R1)	663 Ω	822 Ω	246 Ω	452 Ω	4.82 kΩ
R_{ct} (R2)	35.2 Ω	102 Ω	31.4 Ω	32.3 Ω	205 Ω

Table S2 fitting parameter values of the Nyquist plot obtained via Electrochemical Impedance Spectroscopy. Rs : Solution resistance; $R1$, $R2$: Electrolyte and charge transfer resistance ; CPE : Constant phase element

	Synthesis methodology	$\boldsymbol{\eta\ (j = 10\ mA/cm2)}$	**Tafel slope (b)**	**Reference**
NbSeS (x=0.5)	Hot injection colloidal synthesis	290 mV	75 mV/dec	This work
NbS_2/rGO composite	Solid state synthesis	500 mV	72mV/dec	[11]
P-Se co-doped NbS_2	Liquid-phase phosphating selenization pyrolysis method	363 mV	116.7 mV/dec	[12]
3R NbS_2	Solid state synthesis	467 mV	110 mV/dec	[13]
Li- TFSI treated NbS_2	Solid state synthesis	310 mV	-	[14]
Few layer NbS_2	Electrochemical exfoliation of bulk NbS_2	236 mV	125 mV/dec	[15]
Exfoliated NbSeS and Co doped NbSeS	CVT	346 mV 173 mV	147 mV/dec 64 mV/dec	[16]
Nb_2Se_9 without centrifugation Nb_2Se_9 at 2000 rpm Nb_2Se_9 at 4000 rpm Nb_2Se_9 at 6000 rpm	Flux method Vacuum filtration over porous carbon paper	-310 mV -294 mV -203 mV -170 mV	129.7 mV/dec 108 mV/dec 86.7 mV/dec 82.2 mV/dec	[17]

Table S3 Comparison of HER activity of Nb based dichalcogenide electrocatalysts in 0.5M H_2SO_4.

Vacancy formation energy:

To calculate the defect formation energy (E_f) of the S/Se vacancy, the following expression was used:

$$E_f(vac) = E\ (vac) - E\ (pristine) - \mu(S\ or\ Se)$$

where $E(Vac)$ is the total energy of system with an S or Se vacancy, $E(pristine)$ is the total energy of the system without any defects, and S/Se is the chemical potential of S or Se.

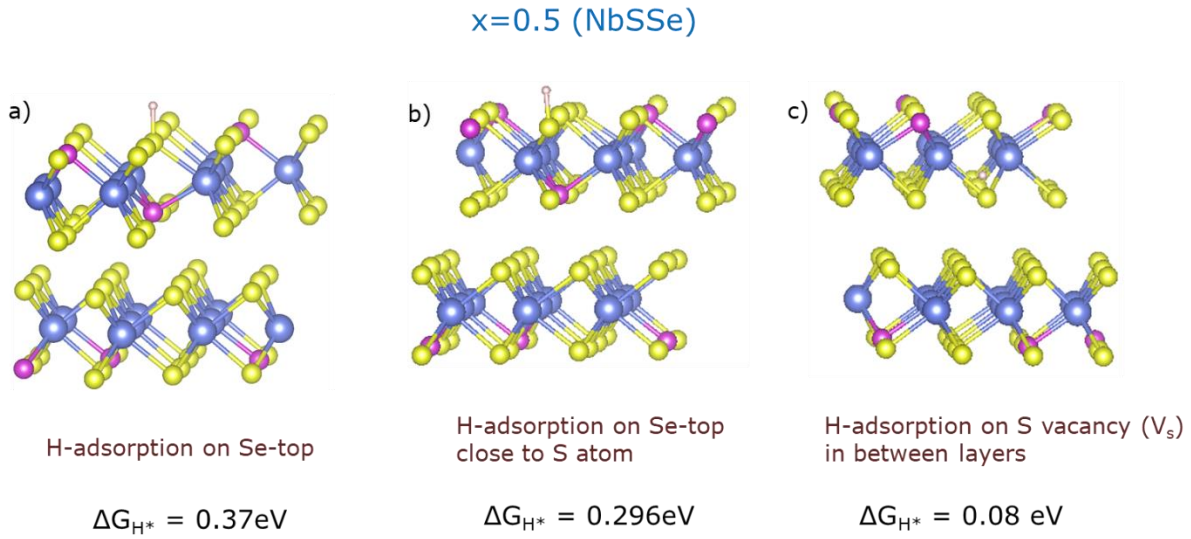

Fig. S10 (a,b) chemical structure of reaction intermediates for H adsorbed on Se_{top} and Se_{top} near S for defect free model in x=0.5 (NbSeS) composition respectively. Lower Gibbs free energy (ΔG_{H*}) value reflects role of polarized electric field in alloy sample due to crystal distortion leading to easy desorption process; (c) reaction intermediate depicting H adsorption on sulphur vacancy (V_s) in between layers.

Gibbs Free Energy Calculations:

By using an equation, we were able to estimate the Gibbs free energy of atomic hydrogen adsorption.

$$\Delta G_H = \Delta E_H + ZPE - T\Delta S_H$$

$$\Delta E_H = E_{\mathrm{Nb(SxSe(1-x))2\ +H}} - E_{\mathrm{Nb(SxSe(1-x))2}} - \frac{1}{2} E_{H_2}$$

ΔE_H represents energy of hydrogen adsorption. The equation considers the difference in hydrogen's zero-point energy and entropy between its adsorbed state and its gas phase.

Post HER Characterization of x = 0.5 (NbSSe):

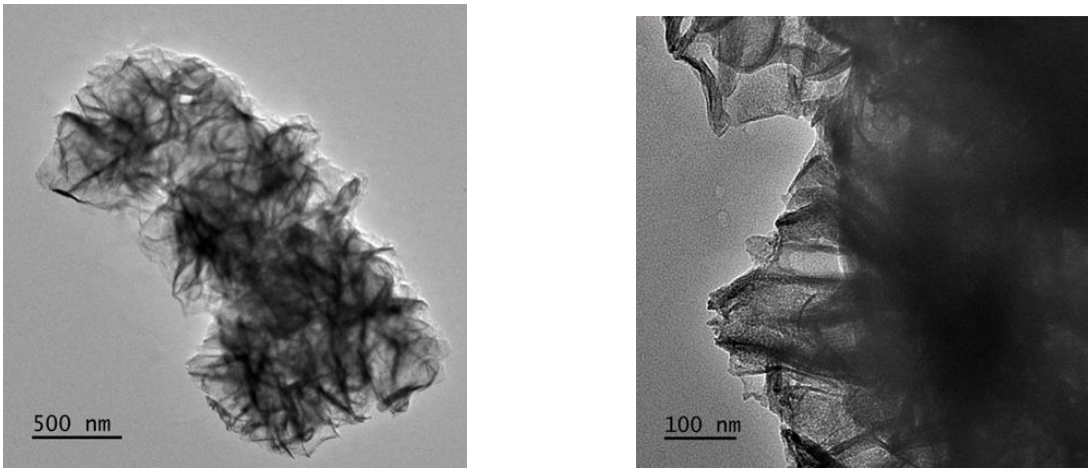

Fig. S11 TEM image of x = 0.5 (NbSSe) after 9 h of chronoamperometry response. TEM image shows that the nanosheet morphology is retained after electro-catalysis.

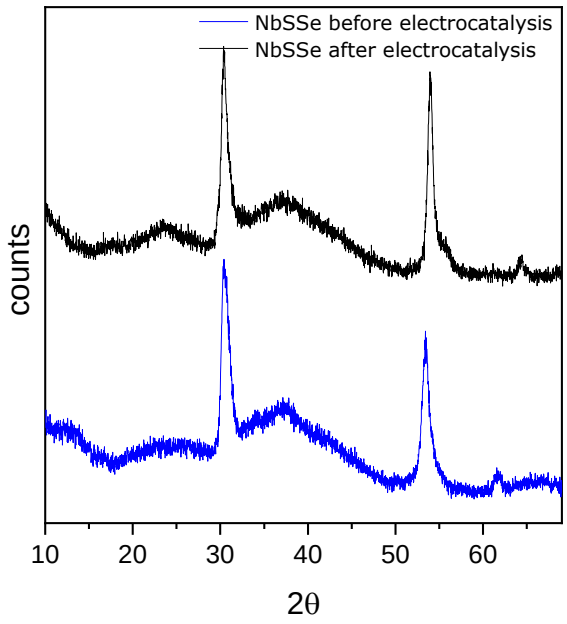

Fig. S12 XRD Pattern before and after electro-catalysis of NbSSe showing no phase change or formation of any other active species. The XRD pattern shows that the catalyst reamins structurally stable during the HER process.

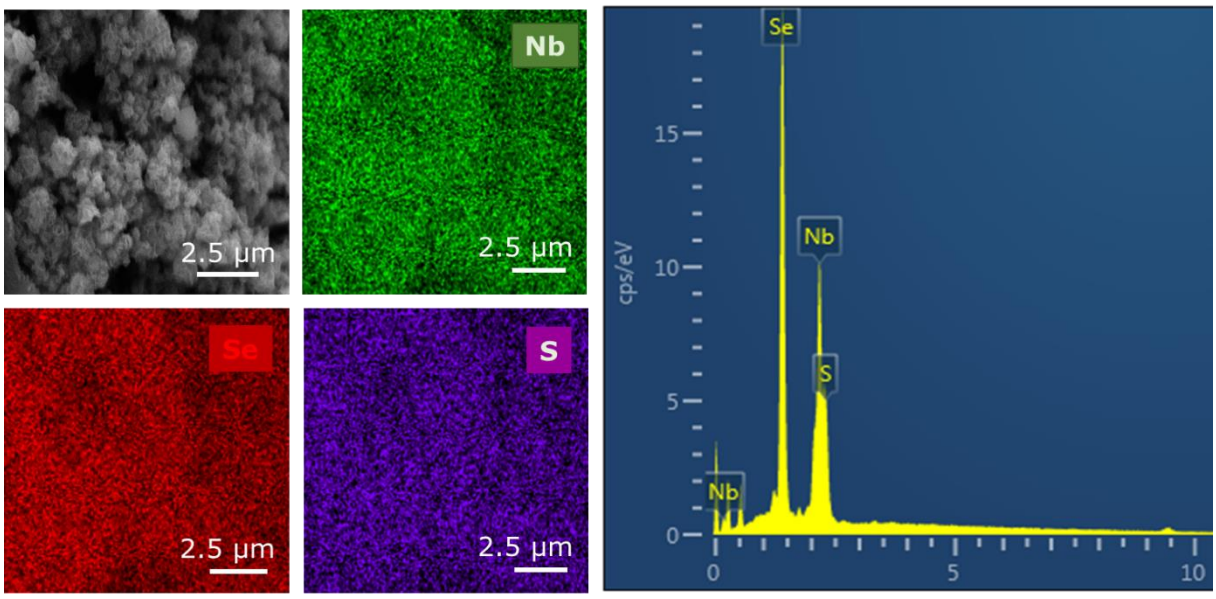

Fig. S13 After electro-catalysis FE-SEM image, corresponding elemental mapping and spectrum of x = 0.5 (NbSSe) showing uniform distribution of elements i.e. Nb, Se and S. The spectrum clearly shows the detected elements are retained after running chronoamperometry response.

References:

1 M. S. Hassan, A. Jana, S. Gahlawat, N. Bhandary, S. Bera, P. P. Ingole and S. Sapra, *Bull. Mater. Sci.*, 2019, **42,** 74.

2 S. Naik, A. Pradhan, A. Mishra and S. L. Samal, *J. Phys. Chem. C*, 2022, **126**, 13762–13773.

3 O. E. Meiron, L. Houben and M. Bar-Sadan, *RSC Adv.*, 2015, **5**, 88108–88114.

4 A. Mansouri and N. Semagina, *ACS Appl. Nano Mater.*, 2018, **1**, 4408–4412.

5 T.L. Cottrell, *The Strengths of Chemical Bonds*, 1958, 41-53.

6 Q. Gong, L. Cheng, C. Liu, M. Zhang, Q. Feng, H. Ye, M. Zeng, L. Xie, Z. Liu and Y. Li, *ACS Catal.*, 2015, **5**, 2213–2219.

7 Q. Fu, L. Yang, W. Wang, A. Han, J. Huang, P. Du, Z. Fan, J. Zhang and B. Xiang, *Adv. Mater.*, 2015, **27**, 4732–4738.

8 R. W. Lord, J. Fanghanel, C. F. Holder, I. Dabo and R. E. Schaak, *Chem. Mater.*, 2020, **32**, 10227–10234.

9 M. S. Hassan, P. Basera, S. Gahlawat, P. P. Ingole, S. Bhattacharya and S. Sapra, *J. Mater. Chem. A*, 2021, **9**, 9837–9848.

10 A. Singh, J. Rohilla, M. S. Hassan, C. Trupthi Devaiah, P. P. Ingole, P. K. Santra, D. Ghosh and S. Sapra, *ACS Appl. Nano Mater.*, 2022, **5**, 4293–4304.

11 D. Gopalakrishnan, A. Lee, N. K. Thangavel and L. M. Reddy Arava, *Sustain. Energy Fuels*, 2018, **2**, 96–102.

12 W. Shen, L. Qiao, J. Ding and Y. Sui, *Appl. Surf. Sci.*, 2022, **581**, 152419.

13 P. Chithaiah, S. Mallick, D. C. Binwal, A. Bhui and C. N. R. Rao, *New J. Chem.*, 2023, **47**, 17098-17102.

14 L. Najafi, S. Bellani, R. Oropesa-Nuñez, B. Martín-García, M. Prato, V. Mazánek, D. Debellis, S. Lauciello, R. Brescia, Z. Sofer and F. Bonaccorso, *J. Mater. Chem. A*, 2019, **7**, 25593–25608.

15 J. Si, Q. Zheng, H. Chen, C. Lei, Y. Suo, B. Yang, Z. Zhang, Z. Li, L. Lei, Y. Hou and K. Ostrikov, *ACS Appl. Mater. Interfaces*, 2019, **11**, 13205–13213.

16 Y. Ren, X. Miao, J. Zhang, Q. Lu, Y. Chen, H. Fan, F. Teng, H. Zhai, X. He, Y. Long, C. Zhang and P. Hu, *J. Mater. Chem. A*, 2023, **11**, 2690–2697.

17 F. O. T. Agyapong-Fordjour, S. Oh, J. Lee, S. Chae, K. H. Choi, S. H. Choi, S. Boandoh, W. Yang, J. Huh, K. K. Kim and J. Y. Choi, *ACS Appl. Energy Mater.*, 2019, **2**, 5785–5792.